


 Cite this: *Chem. Commun.*, 2017, 53, 8372

 Received 8th May 2017,
 Accepted 3rd July 2017

DOI: 10.1039/c7cc03558f

rsc.li/chemcomm

Metal–organic framework derived carbon-confined Ni₂P nanocrystals supported on graphene for an efficient oxygen evolution reaction†

 Manman Wang,^{‡a} Mengting Lin,^{‡a} Jiantao Li,^a Lei Huang,^a Zechao Zhuang,^a Chao Lin,^a Liang Zhou ^{*a} and Liqiang Mai ^{*ab}

Metal–organic framework derived carbon-confined Ni₂P nanocrystals supported on graphene with high effective surface area, more exposed active sites, and enhanced charge transport were successfully designed. The resulting material shows excellent oxygen evolution reaction performance with a remarkably low overpotential of 285 mV at 10 mA cm⁻² and outstanding durability.

The oxygen evolution reaction (OER) is one of the most fundamental and important reactions in many fields such as water splitting and rechargeable metal–air batteries.^{1–3} Generally, this reaction suffers from sluggish kinetics and a large overpotential; thus efficient catalysts are in demand.^{4,5} Although IrO₂ and RuO₂ show high OER performances, their high costs and scarcity severely hinder their practical applications.⁶ Moreover, IrO₂ and RuO₂ may be subject to oxidation during the OER process, leading to the degradation of catalytic activity and an increase of the overpotential.^{7,8} Thus, alternative electrocatalysts are indeed required to make the OER more practically feasible.^{9,10}

Transition metal phosphides (TMPs), such as Ni₂P and CoP, show great potential in realizing efficient oxygen evolution, due to their high conductivity, abundant resources, and long term catalytic stability.^{11,12} While significant progress has been made in promoting the OER performance of TMPs, low chemical durability under a high oxidation potential needs to be conquered. During the OER process, the TMPs can be oxidized to metal oxides/hydroxides/oxyhydroxides easily. On the one hand, the oxidation decreases the electronic conductivity of the TMPs dramatically,^{13,14} which is harmful to the electrocatalytic performance. On the other hand, the metal oxides/hydroxides/oxyhydroxides on the surface of

the TMPs are recognized as active sites for the OER.^{15–17} Thus, a structure which could facilitate the transport of electrons and ensure the occurrence of electrocatalytic reactions should be designed to enhance the OER performance of TMPs. Recently, carbon-confined metal species derived from metal–organic frameworks (MOFs) have drawn growing interest and achieved excellent electrocatalytic performances.^{17,18} Metal-derivatives from MOFs can serve as catalytically active sites. Meanwhile, organic ligands can be converted into graphitized/amorphous carbon matrix, which functions as an electron highway and confines the crystal growth of metal-derivatives.^{19,20} However, the derived carbon often shows an agglomerated morphology, a low degree of graphitization, and unsatisfactory electronic conductivity. In order to achieve high catalytic activity, reducing agglomeration to fully expose the active sites and building an interconnected charge transport highway should be satisfied at the same time.

Herein, we report Ni-MOF derived carbon-confined Ni₂P nanocrystals supported on a graphene (Ni₂P@C/G) structure, and superior OER electrocatalytic performance has been achieved. The Ni₂P@C/G catalyst shows remarkable electrocatalytic activity with an overpotential of 285 mV to generate 10 mA cm⁻² and exhibits great durability during the long-term stability test. Compared with Ni₂P@C, the improved OER performance of Ni₂P@C/G is ascribed to the introduction of graphene, which increases the electrochemically active surface area, exposes more active sites, and enhances the charge transport. The catalytic mechanism and structural evolution of Ni₂P@C/G during the OER test have also been discussed.

The synthesis process of Ni₂P@C/G is illustrated in Fig. 1. Firstly, a Ni-MOF supported on reduced graphene oxide (Ni-MOF/rGO) was prepared by a facile solvothermal method. Then Ni-MOF/rGO was annealed in argon to obtain carbon-confined Ni nanocrystals supported on graphene (Ni@C/G). Finally, Ni@C/G was phosphorized to Ni₂P@C/G. For comparison, a Ni-MOF, Ni@C and Ni₂P@C were also fabricated.

X-ray diffraction (XRD) patterns of the Ni-MOF/rGO and pristine Ni-MOF (Fig. S1, ESI†) are in good agreement with a previous report,²¹ indicating the successful synthesis of Ni-MOF

^a State Key Laboratory of Advanced Technology for Materials Synthesis and Processing, International School of Materials Science and Engineering, Wuhan University of Technology, Wuhan 430070, Hubei, China.
 E-mail: liangzhou@whut.edu.cn, mlq518@whut.edu.cn

^b Department of Chemistry, University of California, Berkeley, California 94720, USA

† Electronic supplementary information (ESI) available. See DOI: 10.1039/c7cc03558f

‡ These authors contributed equally to this work.

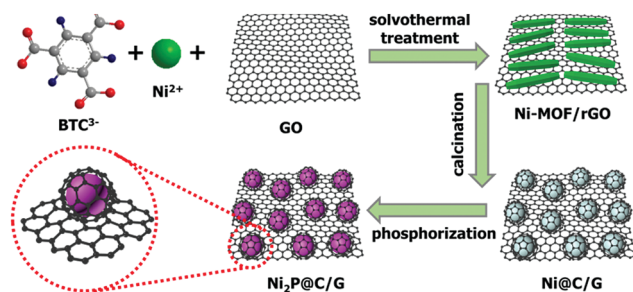


Fig. 1 Scheme for the synthesis of $\text{Ni}_2\text{P}@C/G$.

crystals with/without GO. Scanning electron microscopy (SEM) images of the Ni-MOF/rGO present a sheet-like morphology with needle-like Ni-MOF crystals uniformly dispersed on the surface of rGO (Fig. S2a and b, ESI[†]). The pristine Ni-MOF agglomerates into microspheres with a diameter of $\sim 1.7 \mu\text{m}$ (Fig. S2c and d, ESI[†]), which is also consistent with a previous report.²¹ After being annealed in argon, the products Ni@C/G and Ni@C were acquired and characterized by XRD and SEM. For both samples, all the diffraction peaks can be indexed to pure Ni (JCPDS No. 89-7128) (Fig. S3, ESI[†]), and the morphologies can be generally preserved after annealing (Fig. S4a–d, ESI[†]). Due to the decomposition of Ni-MOF crystals into Ni@C, the needles on the original sheet-like Ni-MOF/rGO disappear and the surface becomes rougher (Fig. S4a and b, ESI[†]), while the spherical structure of the pure Ni-MOF shrinks to $\sim 1.5 \mu\text{m}$ (Fig. S4c and d, ESI[†]).

After phosphorization, $\text{Ni}_2\text{P}@C/G$ and $\text{Ni}_2\text{P}@C$ can be obtained. The XRD results show that both samples are composed of highly pure Ni_2P (JCPDS No. 89-4864) (Fig. 2a). The SEM and transmission electron microscopy (TEM) images of $\text{Ni}_2\text{P}@C/G$ show that the sheet-like structure is retained after phosphorization, and the $\text{Ni}_2\text{P}@C$ nanoparticles are uniformly distributed on the graphene surface without agglomeration (Fig. 2b and c). Fig. 2d clearly

demonstrates that Ni_2P nanocrystals with a size of $\sim 13 \text{ nm}$ are confined within carbon shells (the thickness is $\sim 4 \text{ nm}$). From the high-resolution TEM (HRTEM) image (Fig. 2d, inset), distinct lattice fringes can be observed on the carbon shell, proving the successful formation of graphitized carbon, and a lattice spacing of 0.339 nm corresponding to the (001) plane of Ni_2P is also identified. In contrast, the spherical structure is maintained after phosphorization (Fig. S5a and b, ESI[†]), but $\text{Ni}_2\text{P}@C$ nanocrystals show an agglomerated morphology (Fig. S5c, ESI[†]), and a lattice spacing of 0.506 nm corresponding to the (100) plane of Ni_2P is also observed (Fig. S5c, inset, ESI[†]). Raman spectra show two peaks at ~ 1325 and 1590 cm^{-1} for both $\text{Ni}_2\text{P}@C/G$ and $\text{Ni}_2\text{P}@C$, and the two peaks are ascribed to the characteristic D-band (disorder induced phonon mode) and G-band (graphite band) of carbonaceous materials (Fig. S6, ESI[†]).^{22,23} The peak intensity ratio of the D-band to the G-band (I_D/I_G) is correlated with the graphitization degree of carbon materials.²⁴ The I_D/I_G values for $\text{Ni}_2\text{P}@C/G$ and $\text{Ni}_2\text{P}@C$ are 1.17 and 1.23, respectively, confirming their similar graphitization degrees. Through elemental analysis, the carbon contents in $\text{Ni}_2\text{P}@C/G$ and $\text{Ni}_2\text{P}@C$ are determined to be 22.17 wt% and 11.92 wt%, respectively, and the graphene content in $\text{Ni}_2\text{P}@C/G$ is calculated to be 11.64 wt% (assuming the weight ratio of Ni_2P to MOF derived carbon is constant). The as-prepared $\text{Ni}_2\text{P}@C/G$ exhibits a specific surface area of $86 \text{ m}^2 \text{ g}^{-1}$, much higher than that of $\text{Ni}_2\text{P}@C$ ($19 \text{ m}^2 \text{ g}^{-1}$) (Fig. S7, ESI[†]), resulting from the well dispersion of carbon-confined Ni_2P nanocrystals on graphene.

The OER activities of $\text{Ni}_2\text{P}@C/G$ and $\text{Ni}_2\text{P}@C$ were tested in 1 M KOH solution. The electrocatalytic performances of commercial IrO_2 and graphene (original GO after annealing and phosphorization is denoted as graphene) were also evaluated for comparison. The linear sweep voltammetry (LSV) curves (Fig. 3a) reveal that $\text{Ni}_2\text{P}@C/G$ exhibits the lowest onset potential and delivers the highest current density. Both $\text{Ni}_2\text{P}@C/G$ and $\text{Ni}_2\text{P}@C$ exhibit anodic peaks which are attributed to the oxidation

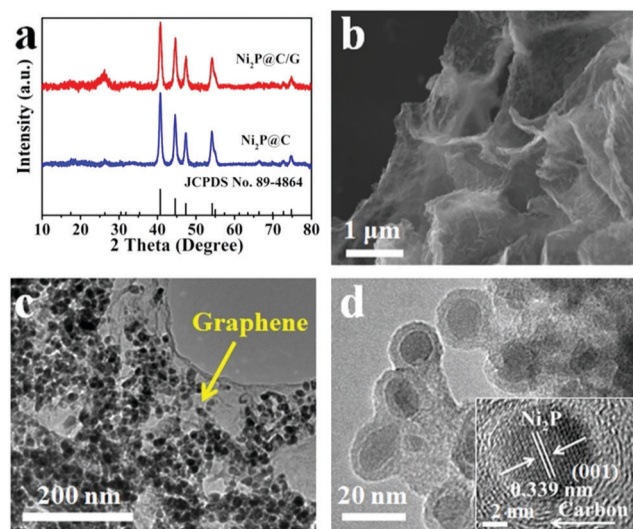


Fig. 2 (a) XRD patterns of $\text{Ni}_2\text{P}@C/G$ and $\text{Ni}_2\text{P}@C$. (b) SEM image of $\text{Ni}_2\text{P}@C/G$. (c and d) TEM images of $\text{Ni}_2\text{P}@C/G$. The inset shows the HRTEM image of $\text{Ni}_2\text{P}@C/G$.

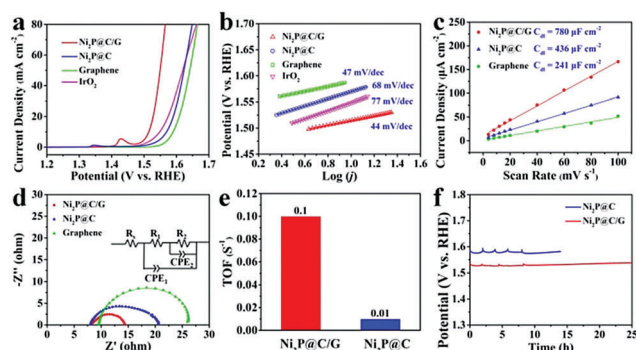


Fig. 3 (a) LSV curves of $\text{Ni}_2\text{P}@C/G$, $\text{Ni}_2\text{P}@C$, graphene and IrO_2 in 1 M KOH at a scan rate of 5 mV s^{-1} . (b) The corresponding Tafel plots for $\text{Ni}_2\text{P}@C/G$, $\text{Ni}_2\text{P}@C$, graphene and IrO_2 . (c) CV current density versus scan rate for $\text{Ni}_2\text{P}@C/G$, $\text{Ni}_2\text{P}@C$ and graphene. The linear slope is equivalent to twice that of the double-layer capacitance (C_{dl}). (d) Nyquist plots for $\text{Ni}_2\text{P}@C/G$, $\text{Ni}_2\text{P}@C$ and graphene. The inset shows the equivalent circuit. (e) The TOF values calculated from the current at an overpotential of 350 mV for $\text{Ni}_2\text{P}@C/G$ and $\text{Ni}_2\text{P}@C$. (f) Durability tests of $\text{Ni}_2\text{P}@C/G$ and $\text{Ni}_2\text{P}@C$ in 1 M KOH at a constant current density of 10 mA cm^{-2} .

of Ni₂P (Fig. S8, ESI†).^{11,17} The overpotential of Ni₂P@C/G is only 285 mV to reach 10 mA cm⁻², much lower than those of Ni₂P@C (340 mV), IrO₂ (320 mV) and graphene (360 mV). These results show that the Ni₂P@C/G catalyst exhibits the highest OER activity.

For investigating the OER kinetics, Tafel plots (Fig. 3b) were analysed. The Tafel slopes are 44, 68, 77 and 47 mV dec⁻¹ for Ni₂P@C/G, Ni₂P@C, IrO₂ and graphene, respectively, which reflects that Ni₂P@C/G shows the fastest kinetics. It is noted that the Tafel slope of graphene is inconsistent with the polarization curve, because they are two different kinetic parameters, and the Tafel slope is mainly used to elucidate the rate-determining step, and this phenomenon has also been observed in previous reports.¹⁷ The OER activities of Ni@C/G and Ni@C were also measured for comparison. The Ni@C/G and Ni@C catalysts show overpotentials of 350 and 380 mV at a current density of 10 mA cm⁻² and Tafel slopes of 84 and 89 mV dec⁻¹ (Fig. S9a and b, ESI†), respectively, which are much higher than those of Ni₂P@C/G and Ni₂P@C. These results indicate that the phosphorization of nickel can largely enhance its electrochemical performances. Moreover, a comparison of Ni₂P@C/G with other reported non-noble OER electrocatalysts is summarized in Table S1 (ESI†); the result implies that Ni₂P@C/G shows outstanding catalytic performance and possesses the potential to realize the practical applications.

To figure out the apparently different performances of Ni₂P@C/G, Ni₂P@C and graphene, electrochemically active surface areas (ECSAs) were estimated from the double-layer capacitance (*C_{dl}*) by conducting cyclic voltammetry (CV) measurements in the non-Faradaic region (Fig. S10, ESI†). As shown in Fig. 3c, the *C_{dl}* value of Ni₂P@C/G is 780 μF cm⁻², 79% higher than that of Ni₂P@C (436 μF cm⁻²) and 223% higher than that of graphene (241 μF cm⁻²), indicating that effective active sites of Ni₂P@C are significantly increased when coupled with graphene.

Electrochemical impedance spectra (EIS) were also obtained to gain insight into the reaction kinetics. Fig. 3d presents the Nyquist plots which were fitted with an equivalent circuit as shown in the inset. The *R_s* mainly results from the solution resistance. *R₁* and *R₂* are associated with the interfacial charge transfer resistance (*R_{ct}* = *R₁* + *R₂*), which can be interpreted as the Faradaic process and oxygen-species adsorption, respectively.^{25,26} The kinetics can be assessed through the *R_{ct}* value: the lower the resistance, the faster the reaction kinetics. Compared with Ni₂P@C (12.7 ohms) and graphene (19 ohms), Ni₂P@C/G shows a much lower *R_{ct}* of 6.5 ohms. The improved charge transport capability of Ni₂P@C/G mainly originates from the interconnected electron highway based on graphitic carbon and graphene; thus higher OER catalytic activity can be achieved.

To assess the intrinsic catalytic activity of Ni₂P@C/G and Ni₂P@C, their turnover frequencies (TOFs) were calculated at an overpotential of 350 mV assuming that all the Ni atoms are catalytically active. The TOF of Ni₂P@C/G is 0.1 s⁻¹, which is 10 times that of Ni₂P@C (0.01 s⁻¹), illustrating enhanced electrocatalytic activity (Fig. 3e).

The long-term stability tests of Ni₂P@C/G and Ni₂P@C were conducted at a constant current density of 10 mA cm⁻². As shown in Fig. 3f, the required potential of Ni₂P@C/G first decreases and

then stabilizes, as the material activation continuously proceeds during the early stage of the OER process. Repeating rises and drops of potential in the first ~8 hours are observed, and this phenomenon is caused by the generation and removal of oxygen bubbles on the electrode surface. Ni₂P@C exhibits a similar performance to that of Ni₂P@C/G, but a higher potential is needed.

To investigate the underlying mechanisms of the Ni₂P@C/G catalyst for the OER, *ex situ* X-ray photoelectron spectroscopy (XPS) was carried out to analyze the surface chemical composition and electronic states before and after the OER test (Fig. 4a and b). The Ni 2p_{3/2} spectrum of Ni₂P@C/G before the OER test exhibits three peaks: the peak at 853.2 eV corresponds to the Ni^{δ+} in Ni₂P, whereas the peak at 856.9 eV can be assigned to the surface oxidized Ni species, and the satellite peak at 861.8 eV is also observed in the Ni 2p_{3/2} region.^{27,28} After the OER test, only one main peak at ~855.6 eV and a satellite peak (861.46 eV) are observed in the Ni 2p_{3/2} spectrum. The main peak can be attributed to Ni(OH)₂ or NiOOH species formed during the OER process according to previous studies.^{29,30} In fact, Ni(OH)₂ will be oxidized to NiOOH within the potential range of the OER;³¹ thus we can ascribe this peak to NiOOH, which will be further proved by *ex situ* TEM. In the P 2p region of Ni₂P@C/G before the OER test, peaks at 129.8 eV and 130.5 eV are in agreement with P 2p_{3/2} and P 2p_{1/2} from Ni₂P,^{27,32} and the peak located at 134.0 eV is attributed to the oxidized P species.^{27,33} After the OER test, the P 2p peaks disappear, which agrees well with a previous report.¹⁷ And this phenomenon might be caused by the transformation of P in Ni₂P into phosphates during the OER and their further dissolution in the electrolyte.¹⁵ The energy dispersive X-ray spectroscopy (EDS) in high-angle annular dark field scanning transmission electron microscopy (HAADF-STEM) mode (Fig. S11, ESI†) was performed to characterize the element distribution before and after the OER process. The EDS elemental

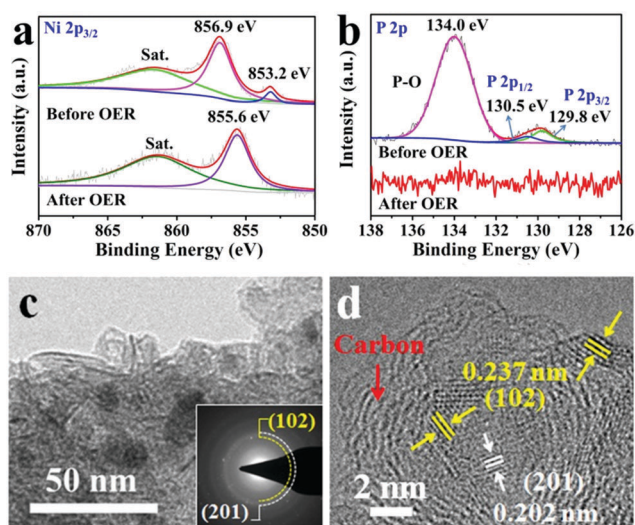


Fig. 4 High-resolution (a) Ni 2p_{3/2} and (b) P 2p XPS spectra of the Ni₂P@C/G before and after the OER process at 10 mA cm⁻² in 1 M KOH for 5000 s. (c) TEM image and SAED pattern (inset) and (d) HRTEM image of the Ni₂P@C/G after the OER stability test in 1 M KOH for 10 h.

mapping images reveal that the phosphorus content decreases after the OER stability test, which further proves the conversion of Ni₂P during the OER process. After the stability test for 10 h, the nanocrystals are still uniformly dispersed on the surface of graphene (Fig. S12, ESI[†]). An *ex situ* TEM image (Fig. 4c) shows the existence of nanosheets after the OER test, which could be attributed to the *in situ* generated NiOOH. The selected area electron diffraction (SAED) pattern (Fig. 4c, inset) also confirms the formation of NiOOH and the (102) diffraction ring of NiOOH can be observed. The (201) diffraction of Ni₂P can also be observed in the SAED pattern, indicating that Ni₂P is not fully oxidized in the 10 hour OER process. Sub-nanocrystals instead of an integrated nanocrystal are observed in the HRTEM image (Fig. 4d). Lattice spacings of 0.237 nm and 0.202 nm presented in the image are assigned to the (102) plane of NiOOH and the (201) plane of Ni₂P, respectively. The HRTEM image also shows that the graphitic carbon shell is well maintained after the long-term stability test, suggesting that the interconnected conductive network based on the graphitic carbon shells and graphene substrate can continuously and effectively ensure electron transport. Based on the above analyses, we can conclude that carbon-confined Ni₂P nanocrystals were partially *in situ* oxidized to NiOOH species which serve as electrocatalytically active sites, and the robust carbon/graphene network enable fast electron transfer, thus resulting in highly efficient OER performance.

In summary, graphene supported carbon-confined Ni₂P nanocrystals were successfully designed. The electrocatalytic performance of Ni₂P@C/G is superior to that of commercial IrO₂, with a remarkably decreased overpotential (285 mV at 10 mA cm⁻²), a considerably low Tafel slope (44 mV dec⁻¹) and outstanding durability. Its excellent electrocatalytic performance for the OER is attributed to the increased electrochemically active surface area, more exposed active sites, and enhanced charge transport. *Ex situ* XPS and TEM results show that the Ni₂P was partially oxidized during the OER process and the *in situ* generated NiOOH presumably enhances the electrocatalytic performance for the OER. This work demonstrates the inspiring applications of carbon-confined transition metal phosphides coupled with graphene for an efficient OER, and other energy conversion and storage fields.

This work was supported by the National Key Research and Development Program of China (2016YFA0202603), the National Basic Research Program of China (2013CB934103), the Programme of Introducing Talents of Discipline to Universities (B17034), the National Natural Science Foundation of China (51521001, 21673171, 51502226), the National Natural Science Fund for Distinguished Young Scholars (51425204), and the Fundamental Research Funds for the Central Universities (WUT: 2016III001, 2016III002, 2017III009, 2017III008). Prof. Liqiang Mai gratefully

acknowledged financial support from the China Scholarship Council (No. 201606955096).

Notes and references

- J. Duan, S. Chen, A. Vasileff and S. Z. Qiao, *ACS Nano*, 2016, **10**, 8738–8745.
- F. Song and X. Hu, *Nat. Commun.*, 2014, **5**, 4477.
- Y. Li, M. Gong, Y. Liang, J. Feng, J. E. Kim, H. Wang, G. Hong, B. Zhang and H. Dai, *Nat. Commun.*, 2013, **4**, 1805.
- C. Guo, Y. Zheng, J. Ran, F. Xie, M. Jaroniec and S. Z. Qiao, *Angew. Chem., Int. Ed.*, 2017, **56**, 8539–8543.
- Y. Zheng, Y. Jiao, Y. Zhu, Q. Cai, A. Vasileff, L. H. Li, Y. Han, Y. Chen and S. Z. Qiao, *J. Am. Chem. Soc.*, 2017, **139**, 3336–3339.
- X. Lu and C. Zhao, *Nat. Commun.*, 2015, **6**, 6616.
- E. Antolini, *ACS Catal.*, 2014, **4**, 1426–1440.
- R. Kötz, H. Lwernerz and S. Stucki, *J. Electrochem. Soc.*, 1983, **130**, 825–829.
- B. Bayatsarmadi, Y. Zheng, A. Vasileff and S. Z. Qiao, *Small*, 2017, **13**, 1700191.
- T. Ling, D. Y. Yan, Y. Jiao, H. Wang, Y. Zheng, X. Zheng, J. Mao, X. W. Du, Z. Hu, M. Jaroniec and S. Z. Qiao, *Nat. Commun.*, 2016, **7**, 12876.
- L. A. Stern, L. Feng, F. Song and X. Hu, *Energy Environ. Sci.*, 2015, **8**, 2347–2351.
- M. Sun, H. Liu, J. Qu and J. Li, *Adv. Energy Mater.*, 2016, **6**, 1600087.
- B. Konkana, J. Masa, A. J. R. Botz, I. Sinev, W. Xia, J. Kossmann, R. Drautz, M. Muhler and W. Schuhmann, *ACS Catal.*, 2017, **7**, 229–237.
- K. Zhou, W. Zhou, L. Yang, J. Lu, S. Cheng, W. Mai, Z. Tang, L. Li and S. Chen, *Adv. Funct. Mater.*, 2015, **25**, 7530–7538.
- M. Ledendecker, X. Yang, M. Antonietti and M. Shalom, *ChemSusChem*, 2016, **9**, 2928–2932.
- P. Wang, F. Song, R. Amal, Y. H. Ng and X. Hu, *ChemSusChem*, 2016, **9**, 472–477.
- X. Y. Yu, Y. Feng, B. Guan, X. W. Lou and U. Paik, *Energy Environ. Sci.*, 2016, **9**, 1246–1250.
- J. Wei, Y. Hu, Z. Wu, Y. Liang, S. Leong, B. Kong, X. Zhang, D. Zhao, G. P. Simon and H. Wang, *J. Mater. Chem. A*, 2015, **3**, 16867–16873.
- A. Mahmood, W. Guo, H. Tabassum and R. Zou, *Adv. Energy Mater.*, 2016, **6**, 1600423.
- H. Tabassum, W. Guo, W. Meng, A. Mahmood, R. Zhao, Q. Wang and R. Zou, *Adv. Energy Mater.*, 2017, **7**, 1601671.
- F. Zou, Y. M. Chen, K. Liu, Z. Yu, W. Liang, S. M. Bhoway, M. Gao and Y. Zhu, *ACS Nano*, 2016, **10**, 377–386.
- D. Pan, J. Zhang, Z. Li and M. Wu, *Adv. Mater.*, 2010, **22**, 734–738.
- Q. Li, Q. Wei, J. Sheng, M. Yan, L. Zhou, W. Luo, R. Sun and L. Mai, *Adv. Sci.*, 2015, **2**, 1500284.
- V. Di Noto, E. Negro, S. Polizzi, K. Vezzù, L. Toniolo and G. Cavinato, *Int. J. Hydrogen Energy*, 2014, **39**, 2812–2827.
- R. L. Doyle and M. E. G. Lyons, *Phys. Chem. Chem. Phys.*, 2013, **15**, 5224–5237.
- J. Kibsgaard, T. F. Jaramillo and F. Besenbacher, *Nat. Chem.*, 2014, **6**, 248–253.
- R. Wei, Q. Zhu, F. Han, Q. Guan and W. Li, *RSC Adv.*, 2015, **5**, 38774–38782.
- J. A. Cecilia, A. Infantes-Molina, E. Rodriguez-Castellon and A. Jimenez-Lopez, *J. Catal.*, 2009, **263**, 4–15.
- X. Yu, T. Hua, X. Liu, Z. Yan, P. Xu and P. Du, *ACS Appl. Mater. Interfaces*, 2014, **6**, 15395–15402.
- D. Liu, Q. Lu, Y. Luo, X. Sun and A. M. Asiri, *Nanoscale*, 2015, **7**, 15122–15126.
- J. W. Lee, T. Ahn, D. Soundararajan, J. M. Ko and J. D. Kim, *Chem. Commun.*, 2011, **47**, 6305–6307.
- Z. Pu, Q. Liu, P. Jiang, A. M. Asiri, A. Y. Obaid and X. Sun, *Chem. Mater.*, 2014, **26**, 4326–4329.
- Q. Guan, X. Cheng, R. Li and W. Li, *J. Catal.*, 2013, **299**, 1–9.